Development of optimum cold-formed steel sections for maximum energy dissipation in uniaxial bending

Jun Ye[1], Jurgen Becque[1*], Iman Hajirasouliha[1], Seyed Mohammad Mojtabaei[1], James B.P. Lim[2]

[1]Department of Civil and Structural Engineering, The University of Sheffield, Sheffield, UK

[2]Department of Civil and Environmental Engineering, The University of Auckland, New Zealand

* Corresponding author, E-mail: j.becque@sheffield.ac.uk

Abstract

Cold-formed steel (CFS) elements are increasingly used as load-bearing members in construction, including in seismic regions. More conventional hot-rolled steel and concrete building structures are typically allowed by the design standards to exceed their elastic limits in severe earthquakes, rendering parameters indicating ductility and energy dissipation of primordial importance. However, insufficient research has yet been conducted on the energy dissipation of CFS structures. In the majority of previous optimization research on CFS sections the ultimate capacity, as typically controlled by local, distortional and/or global buckling modes, is considered to be the sole optimization criterion. This paper aims to improve the seismic performance of CFS elements by optimising their geometric and material highly non-linear post-buckling behaviour to achieve maximum energy dissipation. A novel shape optimisation framework is presented using the Particle Swarm Optimisation (PSO) algorithm, linked to GMNIA ABAQUS finite element analyses. The relative dimensions of the cross-section, the location and number of intermediate stiffeners and the inclination of the lip stiffeners are considered to be the main design variables. All plate slenderness limit values and limits on the relative dimensions of the cross-sectional components as defined by Eurocode 3, as well as a number of practical manufacturing and construction limitations, are taken into account as constraints in the optimisation problem. It is demonstrated that a substantial improvement in energy dissipation capacity and ductility can be achieved through the

proposed optimization framework. Optimized cross-sectional shapes are presented which dissipate up to 60% more energy through plastic deformations than a comparable commercially available lipped channel.

Key words: Cold-formed steel; Shape optimisation; Energy dissipation; Seismic

1 Introduction

Cold-formed steel (CFS) sections are produced by rolling or brake-pressing relatively thin metal sheets into cross-sectional shapes at ambient temperature. Structural systems composed of CFS members provide a wide range of advantages. They typically offer a high strength-to-weight ratio, making efficient use of the material. Moreover, they are lightweight and consequently easy to handle, transport and install. Practical limitations on the sheet thicknesses, however, result in CFS members being susceptible to instabilities such as local, distortional and global buckling. The large width-to-thickness ratios of CFS members also leave them typically outside the limits prescribed by seismic design codes (e.g. AISC 341-16 2016, EN1998-1 2005) for high seismic regions.

It has been shown that optimisation of CFS elements based on their maximum strength under bending or compression can lead to significant material savings. Relevant work has been carried out by, among others, Liu et al. (2004), Tian and Lu (2004), Leng et al. (2014) and Ma et al. (2015).

While research has previously been conducted on the seismic behaviour of CFS stud wall systems (Nithyardan and Kalyanaraman 2012), research into the energy dissipation capacity of individual CFS load-bearing elements is very limited. Calderoni et al. (2009) conducted monotonic and cyclic tests to study the seismic behaviour of CFS channel beams. The results of their study showed a substantial ductility and energy dissipation capacity. The cyclic behaviour of typical CFS wall studs was investigated by Padilla-Llano et al. (2014). The experimental results showed that the amount of energy dissipated by the studs varied with the dimensions and the shape of the profile, but typically decreased with increasing cross-sectional slenderness.

Other research on the development of members for CFS moment-resisting frames has shown that the ductility and energy dissipation of the sections can be significantly improved by curving the flanges into a semi-circular shape (Sabbagh et al. 2012). However, such curved flanges are difficult to manufacture and provide challenges when connecting them to floor elements. More practical shapes can be developed by taking into account manufacturing and construction constraints, as demonstrated by Ye et al. (2016a) and Ye et al. (2016b).

In other relevant research Pan et al. (2007) developed an optimisation method to obtain hot-rolled H-beams with optimal flange shapes which maximize the energy dissipation capacity of the members under monotonic and cyclic loads. To achieve this, they combined a Simulated Annealing optimisation algorithm with detailed nonlinear finite element analyses.

The fact that the production process of CFS members is relatively straightforward and versatile offers great scope for the development of new, innovative and optimised cross-sections. A novel framework is therefore proposed in this paper to optimise CFS sections with respect to their energy dissipation capacity under monotonic loading. The relative dimensions of the cross-sections, the location and the number of intermediate stiffeners and the inclination of the lip stiffeners were thereby considered as the main design variables. To obtain the global optimum solution a Particle Swarm Optimisation (PSO) algorithm was combined with the general purpose finite element program ABAQUS v6.14 (2014), which was used to carry out geometric and material non-linear analyses including the effects of initial imperfections (GMNIA).

2. Scope and range of prototype sections

In the design of hot-rolled steel members for high seismic regions, the width-to-thickness ratios of compressive elements are limited by codes of practice (AISC 341-16 2016, EN1998-1 2005) to allow for the development of sufficient plastic deformations. As expected, CFS members generally do not satisfy these limits. However, unlike hot-rolled steel members, intermediate stiffeners and

lips can be rolled into CFS members to suppress cross-sectional instabilities (Fig. 1). Adding a lip stiffener is a very effective way to stabilize the top flange of cross-sections subjected to bending (Fig. 1(a)), while an additional intermediate stiffener in the flange (Fig. 1(b)) is useful for wide flanges. For slender webs with high width-to-thickness ratios local buckling may be initiated in the web and an intermediate web stiffener may therefore increase the flexural performance (Fig. 1(c)).

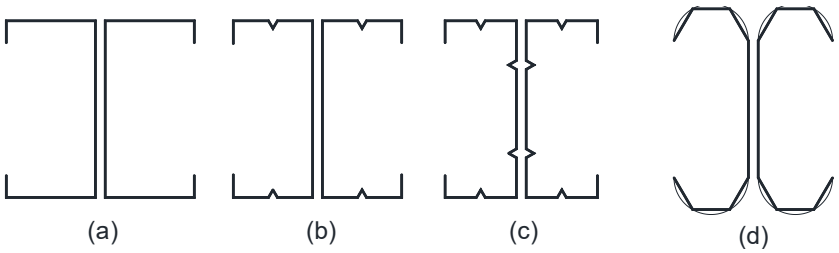

Fig. 1. Cross-section prototypes

In addition to sections (a)-(c) in Fig. 1, the 'folded flange' section pictured in Fig. 1(d) was also considered as a prototype in the proposed optimization procedure. This cross-section was previously developed and studied by Ye et al. (2016b) and originated from a practical approximation of a curved flange section. The study provided additional design guidance to determine the bending capacity of this section to EN1993-1-3 (2005), accounting for the possible occurrence of multiple distortional buckling modes. Furthermore, the paper reports on an optimization study where the Particle Swarm Optimisation (PSO) algorithm was employed to maximise the flexural strength of various prototypes, including the sections shown in Fig. 1(a)-(c), as well as the folded flange section. The results showed that, for the same amount of material, the folded flange section provided a bending capacity which was up to 57% higher than other optimized shapes, as illustrated in Fig. 2. Consequently, it is an obvious candidate to be considered in the current optimization study.

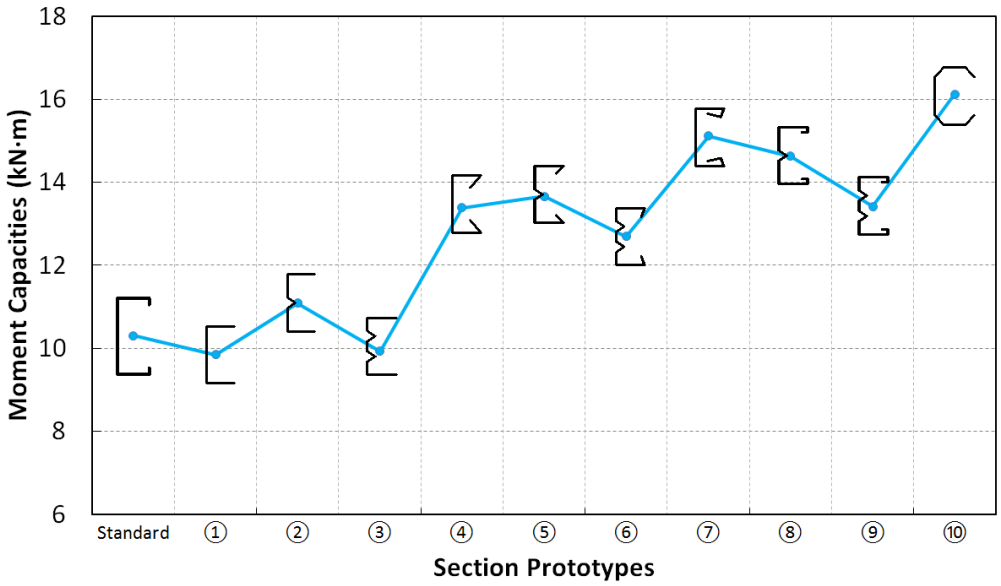

Fig. 2. Comparison of the flexural capacities of optimum CFS prototypes (after Ye et al. 2016b)

3 FE analyses of CFS beams

Previous research studies have shown that finite element (FE) models can be used to accurately predict the load carrying capacity and post-buckling behaviour of CFS sections, provided that the appropriate element type, material parameters and imperfection profiles are selected (Haidarali and Nethercot 2011, Yu and Schafer 2007, Becque and Rasmussen 2009a 2009b). In this paper, the general purpose FE package ABAQUS v6.14 (2014) was used, after validation, to predict the deformation behaviour of the prototype beams and to search for the optimum cross-sectional shapes which maximize the energy dissipation.

3.1 FE model and validation

The modelling techniques used in the FE models were first verified against a series of tests on CFS back-to-back channels described by Ye (2016). Six specimens were tested in four-point bending and failed by interaction of local and distortional buckling in the constant moment region. The specimens were laterally supported near the loading points to prevent global instability due to lateral-torsional buckling. The test set-up is schematically shown in Fig. 3. All specimens had a span length of 3100 mm, while the constant moment span was 1200 mm long. Three different cross-

sections were considered (Figure 4) and two specimens of each cross-section were tested. The wall thickness of all specimens was 1.5 mm. The channels were connected above the end supports and under the loading points by M12 bolts, but the constant moment span did not feature any connectors. The material properties and the specimen imperfections were accurately measured and details of the measuring procedure, as well as full results, can be found in Ye (2016). The average measured yield stress was 422 MPa.

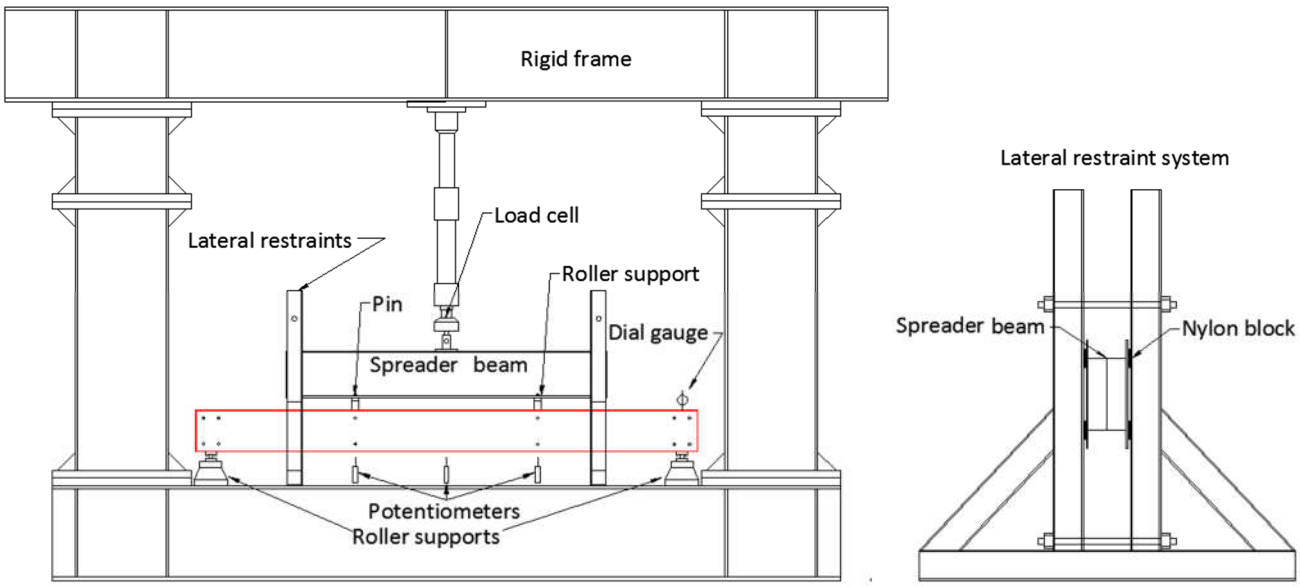

Fig. 3. Test set-up (Ye 2016)

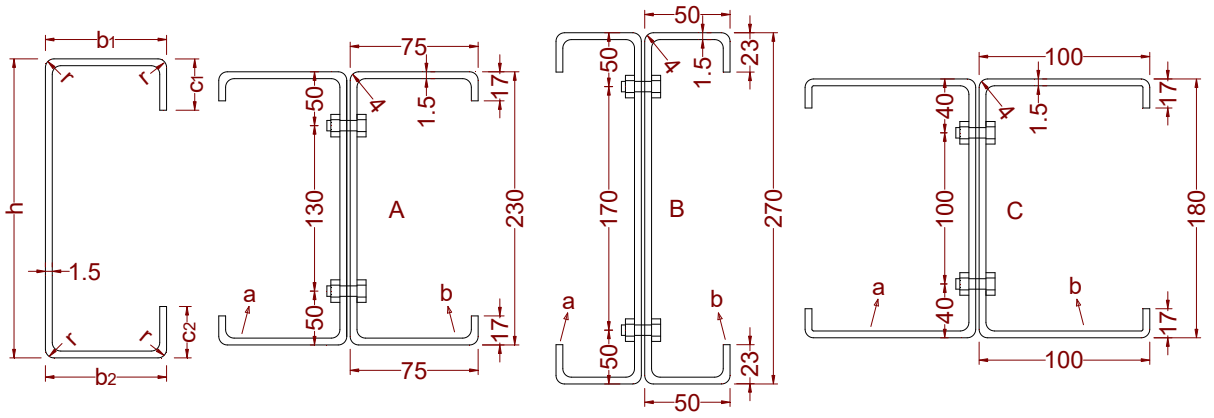

Fig. 4. Cross-sectional dimensions (Ye 2016)

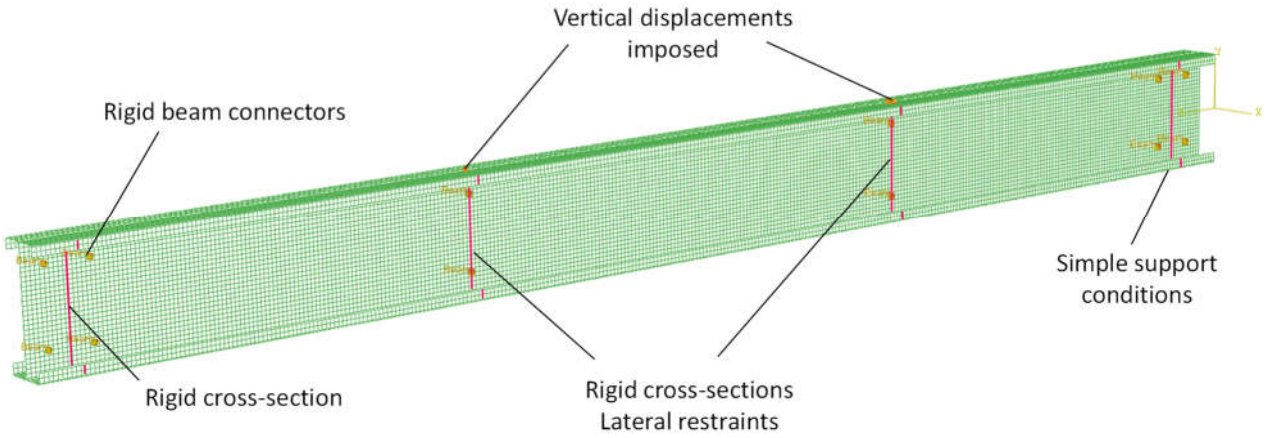

Fig. 5. FE model

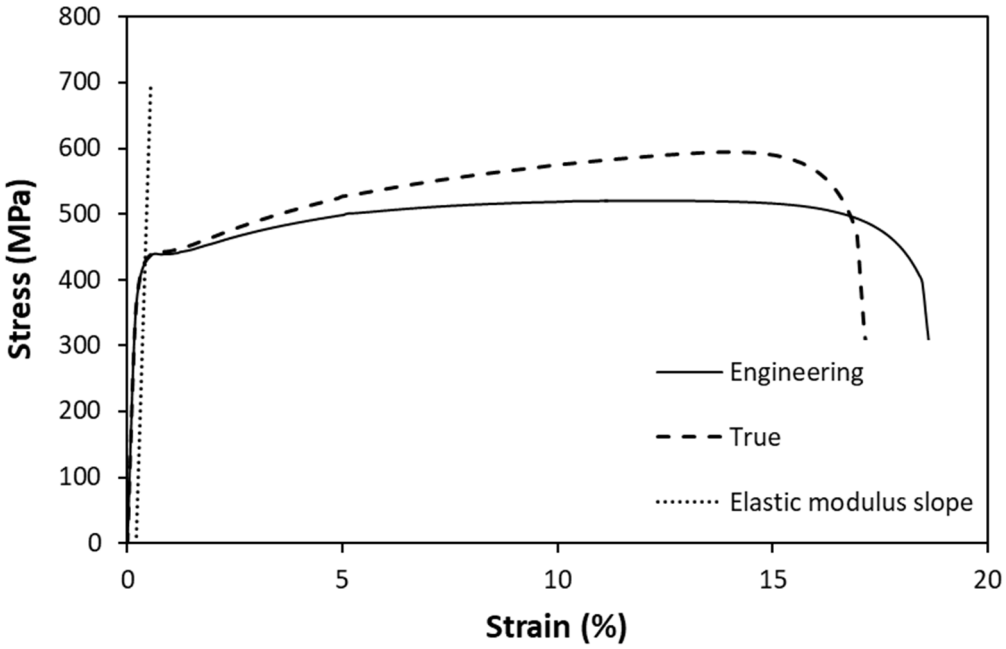

Fig. 6. Material stress-strain curve

The FE models of the CFS beams were developed using 8-node quadrilateral shear-flexible shell elements with reduced integration and five nodal degrees of freedom (S8R5). Figure 5 illustrates the features of the FE model. Rigid cross-sections were defined over the end supports and under the loading points to simulate the wooden blocking used in the test to prevent localized failure by

web crippling. The out-of-plane deformations of the beam were restrained at the supports and at the loading points. Surface-to-surface contact was modelled between the webs of the channels. The bolts were modelled using rigid BEAM connector elements. The measured imperfection profile was transferred into the model by adjusting the initial nodal coordinates. The material was modelled using the measured stress-strain curve, converted from engineering stress and strain to true stress and strain, as shown in Fig.6. The measured material properties were: elastic modulus E = 200 GPa, yield stress f_y = 427 MPa and tensile strength f_u = 593 MPa. A geometrically non-linear 'static general' analysis was carried out.

Residual stresses and the effects of work hardening as a result of the rolling process were not included in the model, based on the observation that they have to some extent opposite effects and based on the recommendation by Schafer et al. (2010) that both phenomena are not independent and that they should therefore either be modelled together or ignored together. Moreover, all sections considered in the study were open sections, in which residual stresses are typically limited.

A mesh sensitivity study was performed using the 180 mm deep specimen indicated in Ye (2016) as C180-1. Four different meshes were considered, containing square elements with 40 mm, 30 mm, 20 mm and 10 mm sides. The results are presented in Fig. 7 in the form of mid-span moment vs. deflection diagrams. The experimentally obtained curve is also shown. It is seen that a mesh refinement to at least 20x20 mm^2 elements is required in order to obtain a good correspondence with the experiment in terms of peak load and overall behaviour.

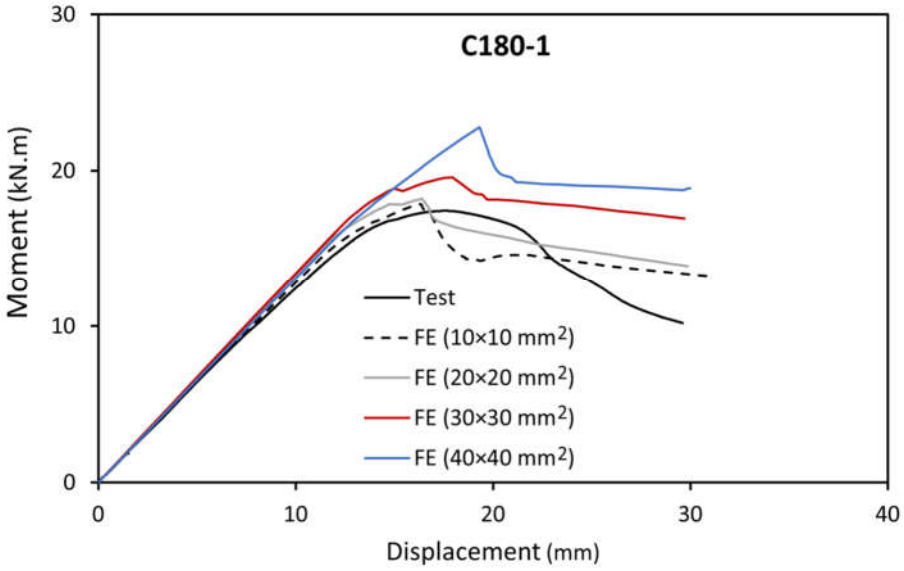

Fig. 7. Results of FE mesh sensitivity study

FE models of all six specimens were constructed and their predictions are compared to the experimentally recorded behaviour in Fig. 8. The specimen labels refer to the cross-section type (A, B or C, with reference to Fig. 4), the cross-section depth (in mm) and the test number (twin specimens were tested).

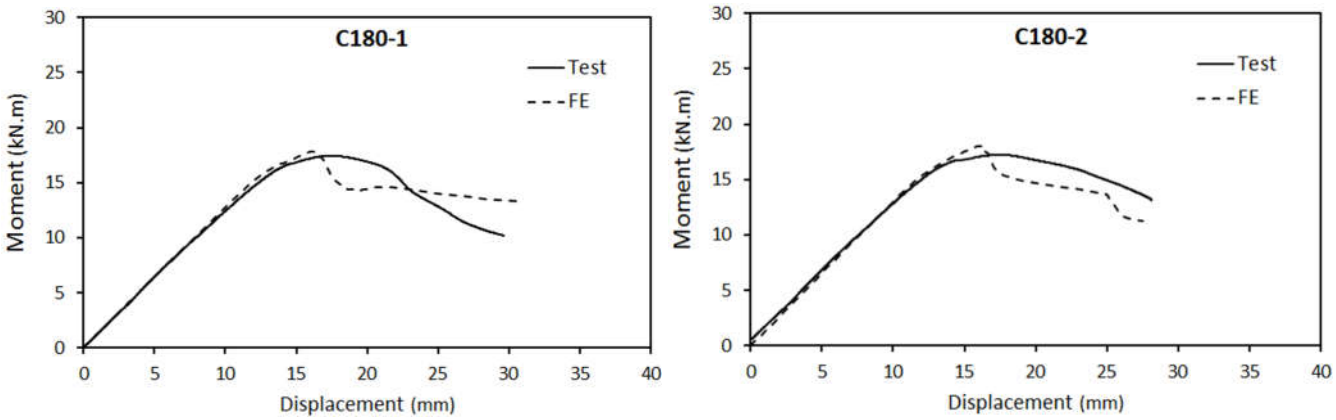

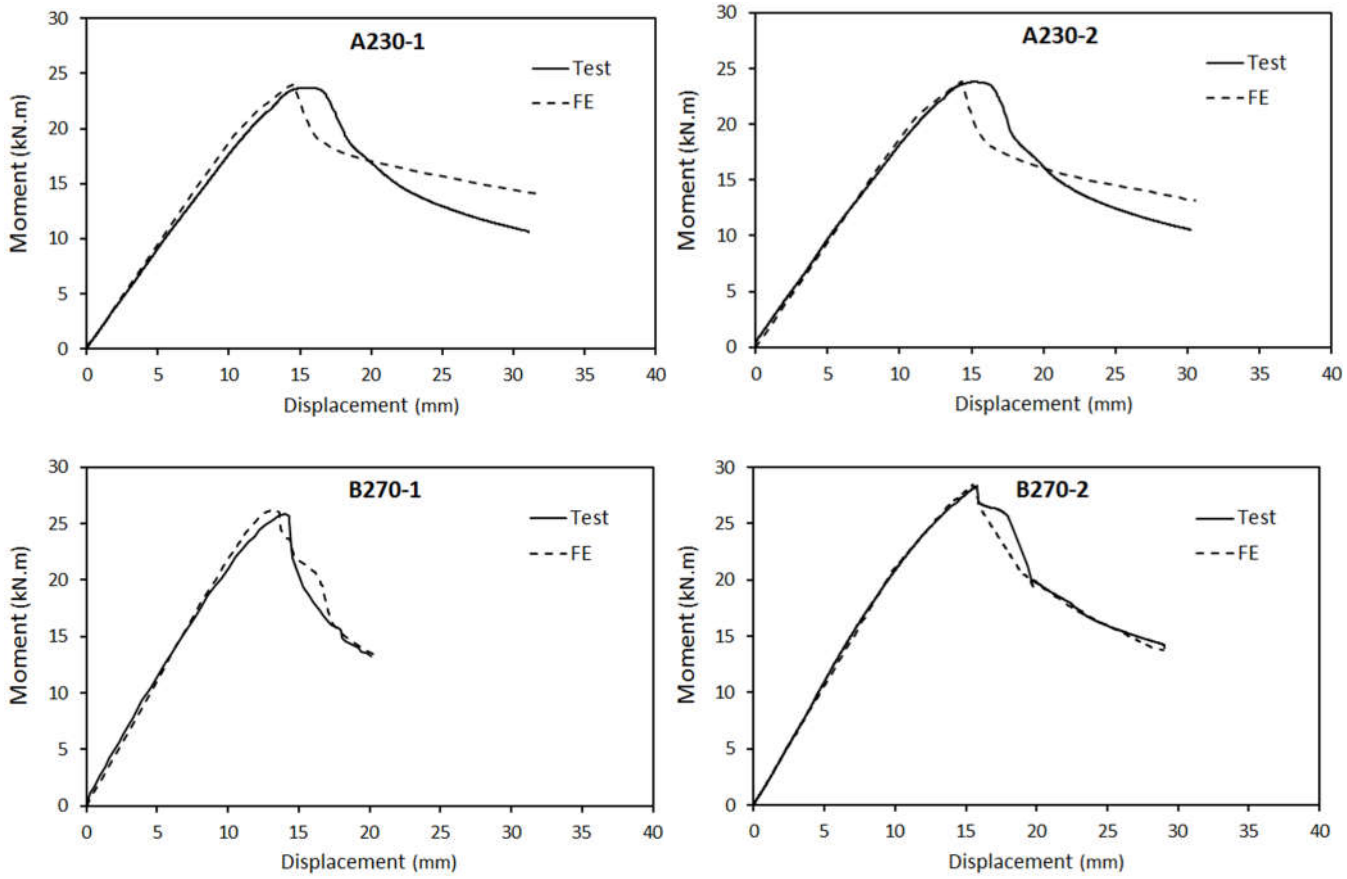

Fig. 8. Comparison of FE results with experimental behaviour

Table 1. Comparison of FE predicted and experimentally recorded peak moment

Specimen	Moment capacity (kNm)		Ratio
	Test	FE	FE/Test
C180-1	17.43	17.86	1.024
C180-2	17.24	18.02	1.045
C230-1	23.72	23.97	1.010
C230-2	23.79	23.87	1.003
C270-1	25.83	26.17	1.013
C270-2	28.34	28.47	1.005
		Average	1.017
		Standard Dev.	0.016

Table 1 compares the FE predicted moment capacity to the experimentally obtained results. It is seen that very good agreement was achieved: the average ratio of the predicted to the measured moment capacity was 1.017 with a standard deviation of less than 2%. However, given that the aim of this paper is to optimize CFS structural members with respect to their energy dissipation capacity, the ability of the FE models to capture the post-peak behaviour with sufficient accuracy is also of primordial importance. This presents a significant challenge because CFS members quite often display interaction between various buckling modes. In the experimental programme here used for validation this pertains to local-distortional interaction. Buckling interaction typically results in a highly unstable post-peak behaviour which displays very high imperfection sensitivity (van der Neut 1969, Becque 2014). This is also observable in Fig. 8, where twin specimens (e.g. C180-1 and C180-2) display a somewhat different post-peak behaviour as a result of the difference in initial imperfections (although the overall trend is similar). Nevertheless, it is seen from Fig. 8 that the FE models predict the overall post-peak behaviour of the test specimens with reasonable accuracy. In the case of the 270 mm deep channels (B270-1 and B270-2) the agreement is excellent with the predicted load-displacement curve following the experimental curve very closely. The area under the curve, which can be deemed an approximate proportional measure of the dissipated energy, is also well represented by the FE models, with an average difference with the experiment over the six specimens of 3% and a maximum difference of 9% (A230-1). For the purpose of the optimization process comparative behaviour is important, e.g. the fact that the 270 mm deep channels display a much steeper post-peak behaviour than the 180 mm deep channels, and in this context it can be concluded that the developed FE techniques provide a sufficiently accurate tool set.

3.2 Flexural strength and post-buckling behaviour of prototypes

A preliminary numerical study was carried out using six different prototype cross-sections (Fig. 9) with the aim of investigating the effect of different cross-section geometries (and in particular the effect of adding intermediate stiffeners) on the general buckling and post-peak behaviour of the section. Fig. 9 shows the dimensions of the six CFS prototype beams, which include two conventional back-to-back lipped channel configurations (C1 and C2), one back-to-back lipped channel configuration with intermediate flange stiffeners (C3), one back-to-back lipped channel configuration with both intermediate web and flange stiffeners (C4), one back-to-back configuration with curved flanges (C5) and one back-to-back configuration with folded flanges (C6). To allow some measure of comparison, all cross-sections used the same amount of material (i.e. they had the same thickness of 3 mm and total developed length of 450 mm) and they all had a 200 mm deep web (with the exception of cross-section C2 which was meant to be compared to C1 to reveal the effect of increasing the web height and narrowing the flanges). All six cross-sections were modelled in back-to-back configurations, in part because this is the arrangement typically encountered in CFS moment resisting frames, and in part to avoid torsion in the sections resulting from the load being applied eccentrically with respect to the shear centre. The webs of both sections were connected along discrete lines at the ends and at the mid-section of the beam using 'tie'-constraints (Fig. 10).

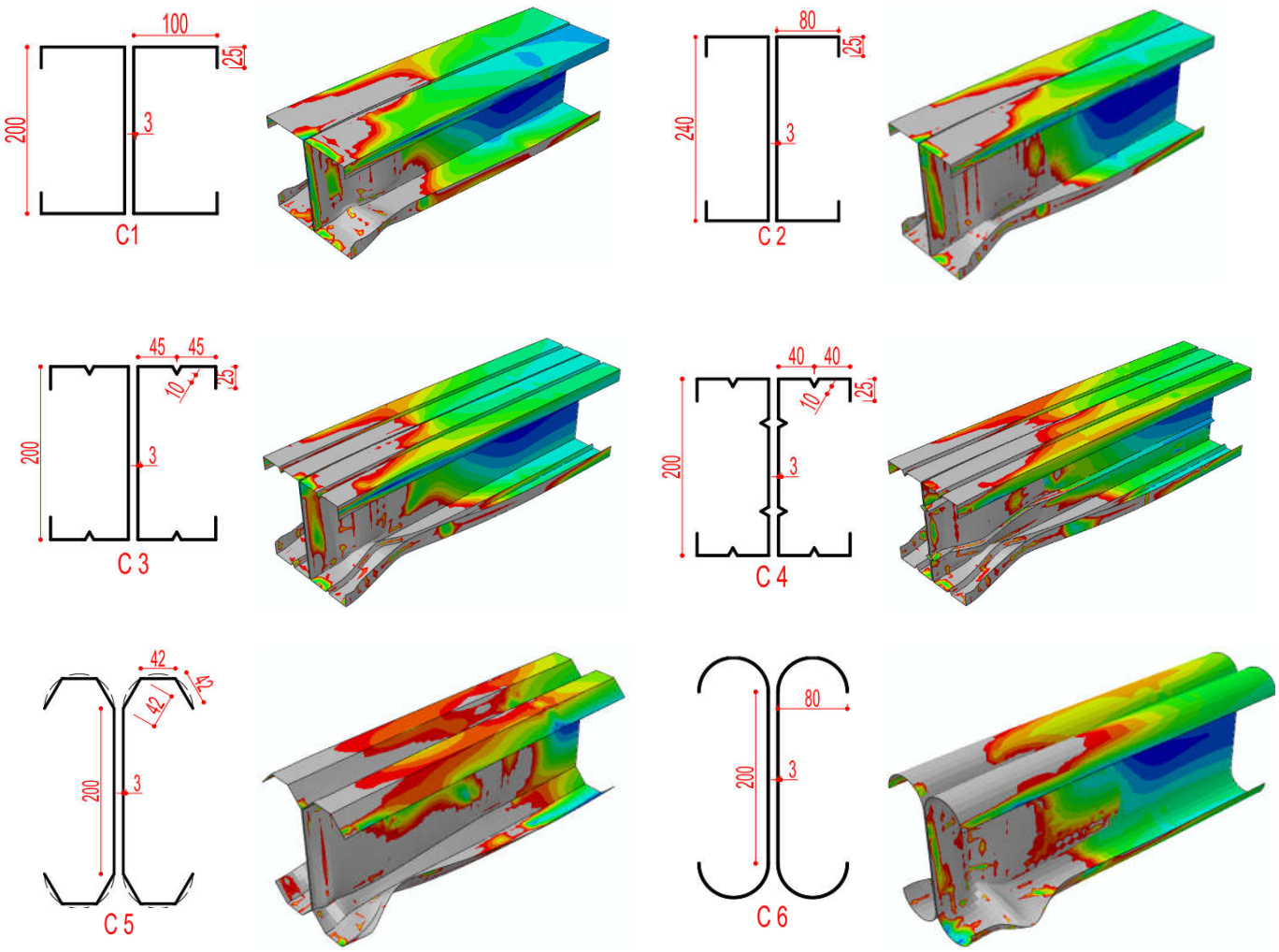

Fig. 9. Cross-sectional shapes and their deformations at a drift angle of 0.04 rad (SMF limit)

A two meter long cantilever beam was modelled, as this was judged to be more representative of the portion of an actual member in a laterally loaded moment-resisting frame between the point of inflection and the beam-to-column connection than a four-point bending arrangement. The beam was laterally restrained to avoid lateral-torsional instability. Figure 10 illustrates the details of the FE model, including the mesh, boundary conditions and lateral restraints. A 20x20 mm^2 mesh was used.

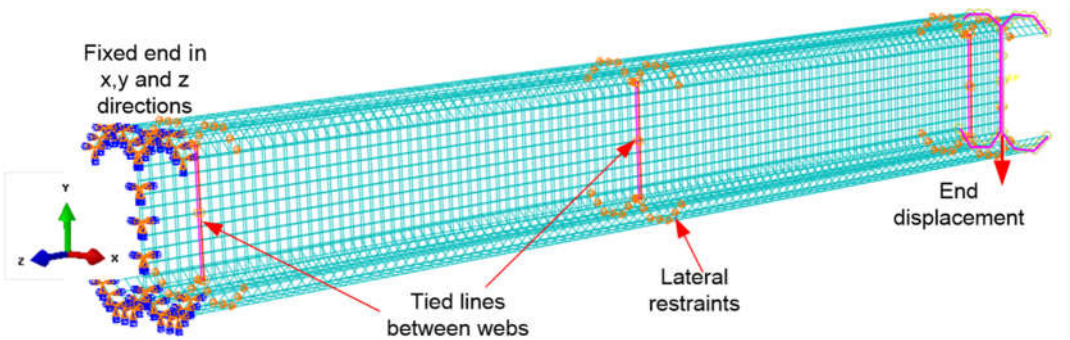

Fig. 10. Mesh, boundary conditions and loading of the beam model

The measured material stress-strain curve shown in Fig. 6 was used in the simulations.

Geometric imperfections were also included in the FE model, using the lowest eigenmode from a buckling (linear perturbation) analysis. The amplitudes of the local and distortional imperfections were taken from Schafer and Pekoz (1998) and were 0.34t and 0.94t, respectively, where t is the wall thickness of the section. These are the 50% values in the cumulative distribution function of measured imperfection amplitudes.

The AISC Seismic Provisions (2016) make a distinction between Intermediate Moment Frames (IMF) and Special Moment Frames (SMF), in part depending on whether they can sustain at least 80% of their peak load carrying capacity at inter-storey drift angles of 0.02 and 0.04 rad, respectively. To determine whether the CFS beam sections under consideration could potentially qualify for either designation, GMNIA modelling was carried out where a vertical displacement of 150 mm (equivalent to a drift angle of 0.075 rad) was imposed at the tip of the cantilever beam (see Fig. 10). Fig. 9 shows the deformations of all six CFS beams at a drift angle of 0.04, while Fig. 11 shows the moment-rotation curves of the beams. It is seen that there is a sudden loss in flexural capacity for the lipped channel C1 well before a rotation of 0.02 rad is achieved due to distortional buckling of the flanges, followed by local buckling. By reducing the width of the flanges and increasing the height of the section in C2, the flexural strength was improved by 25%. However, this did not

substantially improve the general post-buckling behaviour of the section. Fig. 11 also shows that the CFS section with an intermediate stiffener in the flanges (C3) had a slightly higher flexural capacity (by about 10%) compared to the corresponding section without stiffeners (C1), but exhibited considerably less post-buckling strength degradation. A comparison of sections C3 and C4 shows that adding intermediate web stiffeners further improved the post-buckling behaviour of the CFS section, while it had a negligible effect on the flexural strength. The results also demonstrate that, for the same amount of material (i.e. the same thickness and coil width), the curved flange and folded flange sections provided the highest flexural capacity compared to other sections, confirming the results of Ye et al. (2016b).

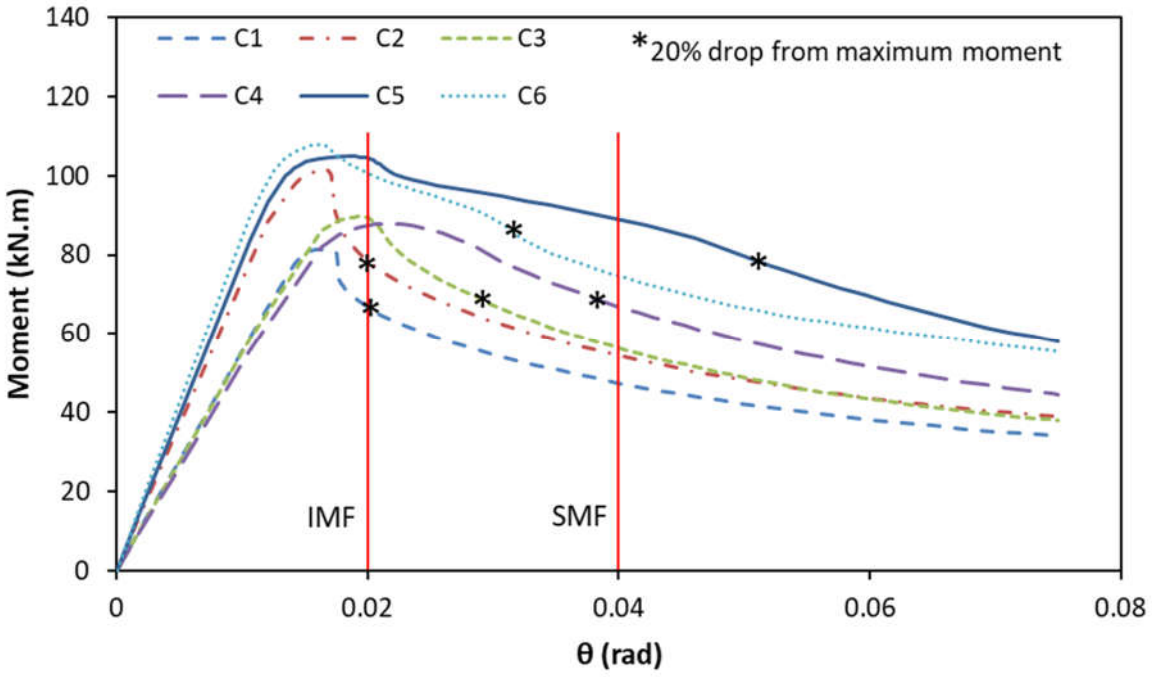

Fig. 11. Moment-rotation curves of beams with dimensions shown in Fig.9

It can be concluded from Fig. 11 that, while sections C1 and C2 satisfied the drift requirement of an IMF, they did not satisfy the SMF drift limits. When adding intermediate stiffeners in the flange, section C3 still did not satisfy the SMF drift requirement due to premature

buckling of the web. However, when using intermediate stiffeners in both the flanges and webs (C4), the CFS section came close to satisfying the SMF inter-storey drift angle requirement. Only the folded flange section (C5) was able to reach a rotation in excess of 0.04 rad without any significant drop in strength. The curved flange section (C6) did not meet the SMF requirement, although its overall moment-rotation behaviour, in qualitative terms, was close to that of C5.

3.3 Cross-section ductility

In accordance with ASTM E2126-09 (2009), the ductility of the six selected sections was evaluated using the equivalent energy elastic-plastic (EEEP) bi-linear model, as shown in Fig. 12. This model idealizes the moment-rotation behaviour of the cross-section into an elastic-perfectly plastic response. The idealized bi-linear curve is obtained by equating the areas A_1 and A_2 included between the idealized and the actual curves and located below and above the actual curve, respectively. The elastic part of the EEEP curve is defined using an initial secant stiffness (K_e) determined by the moment equal to 40% of the idealised yield moment of the cross-section. The ultimate rotation θ_u is then determined by the point on the softening branch of the actual curve corresponding to a 20% drop in moment carrying capacity relative to the peak moment.

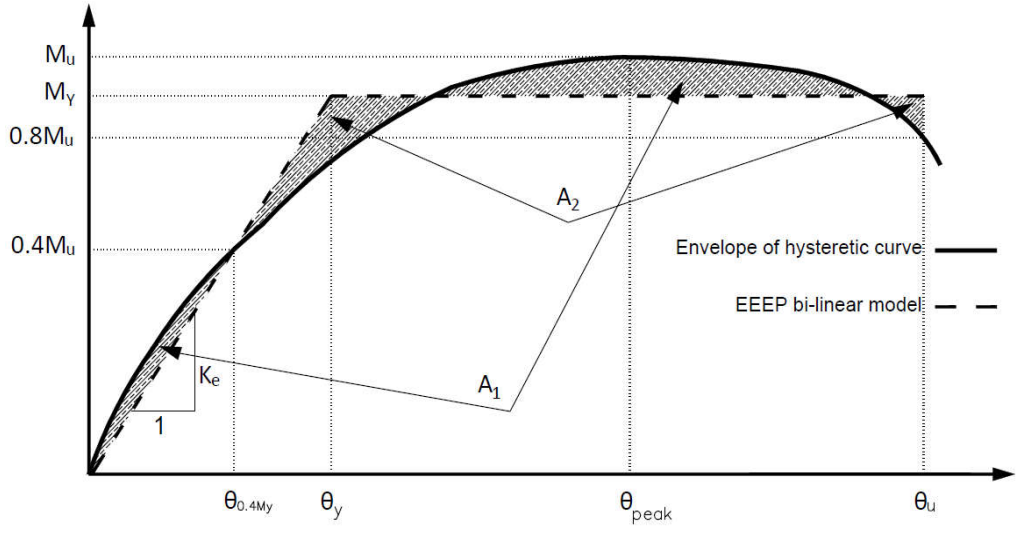

Fig. 12. Equivalent energy elastic-plastic (EEEP) bi-linear model

To investigate the effect of the cross-sectional shape on the ductility of CFS beams, the bi-linear moment-rotation curves were used to calculate the ductility of the CFS sections using the following equation:

$$\mu = \frac{\theta_u}{\theta_y} \tag{1}$$

where θ_y is the yield rotation in the equivalent bi-linear diagram, as shown in Fig. 12. The ductility of the six selected beam sections (with the specifications shown in Fig. 9) is compared in Fig. 13. The results indicate that, in this case, adding intermediate stiffeners in the flange (C3) increased the ductility of the CFS beam sections by 18% compared to the standard section (C1). By comparison, using intermediate stiffeners in both the web and the flanges (C4) increased the ductility by 51% relative to C1. It can also be seen that, for the same amount of material, the folded flange (C5) and curved flange (C6) sections exhibited much better ductility than the standard channel sections. It should also be noted that the folded flange section C5 offers a more practical solution from the manufacturing and construction point of view than C6. In particular, it is much easier to connect steel decking to the flat flanges of C5 than to the curved flanges of C6.

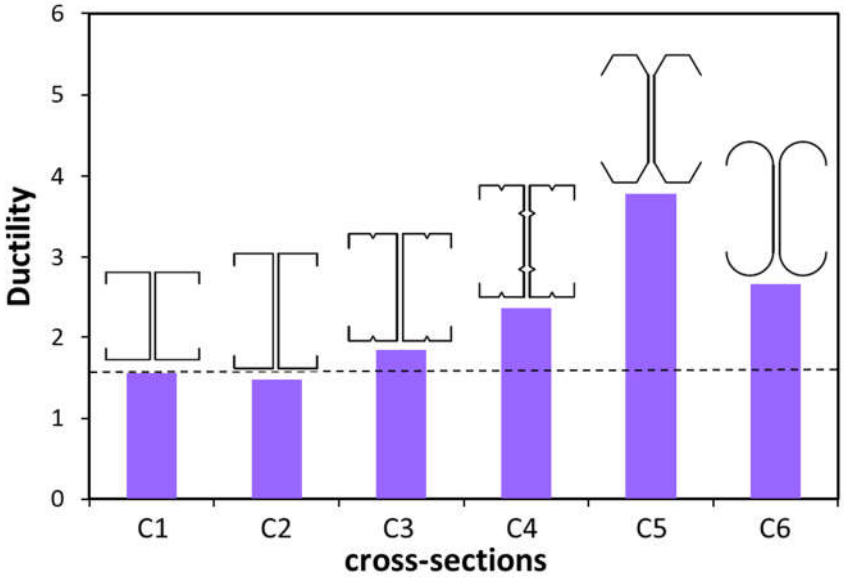

Fig. 13. Ductility of CFS beams with dimensions shown in Fig. 9

3.4 Energy dissipation capacity

The total energy dissipation through plastic deformations can be obtained from the ABAQUS output and is based on the following equation:

$$E = \int_V \int_0^t \sigma_{ij}(\tau)\dot{\varepsilon}_{ij}^{p}(\tau)d\tau dV \quad (2)$$

Where V is the total volume of the beam, t is the duration of loading, σ_{ij} are the components of the stress tensor and $\dot{\varepsilon}_{ij}^{p}$ are the incremental plastic strains. Fig. 14 presents the dissipated energy calculated according to Eq. (2) at a drift ratio of 4% (i.e. the SMF limit) for all six CFS prototypes.

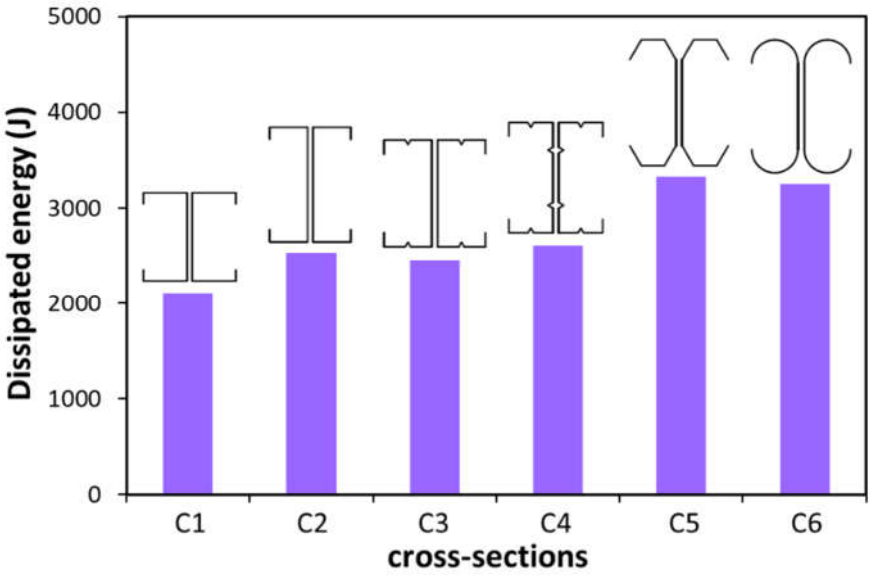

Fig. 14. Comparison of dissipated energies for cross-sections shown in Fig. 9

Fig. 14 indicates that the deeper sections are able to dissipate considerably more energy (due to their higher moment capacity), while the addition of flange and/or web stiffeners in the 200 mm deep sections also has a beneficial effect on the energy dissipation capacity (mainly due to their beneficial influence on the post-peak behaviour). The curved and folded flange sections were able to dissipate the most energy.

4 Proposed optimisation framework

The optimization procedure aimed to develop cross-sectional shapes for CFS beams which, for a constant developed length (coil width) and given thickness, maximize the energy dissipation capacity. A commercially available lipped channel section, shown in Fig. 15, was taken as the starting point, with the optimisation process allowing for the addition of inclined lips and rolled-in intermediate stiffeners in the flanges and the web to form more complex cross-sections. The position of the web stiffeners was also made variable in the optimisation process. In addition, the folded flange prototype was considered, based on its favourable performance in Section 3, showing that it has the potential to dissipate high levels of energy. In the optimization process the energy dissipation capacity was determined based on the results from detailed GMNIA FE models.

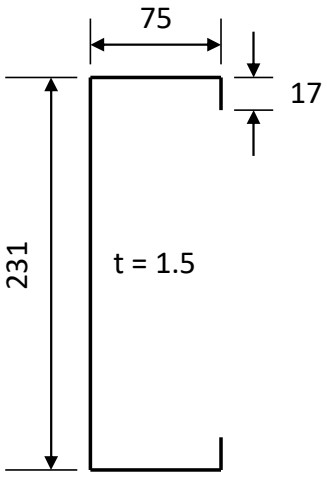

Fig. 15. Dimensions (in mm) of commercial CFS channel

4.1 Problem formulation

Given that the optimization work presented in this paper required several tens of thousands of FE analyses, the cantilever model in Fig. 10 was further simplified. The cantilever length was reduced to 1400 mm and a single channel was modelled. The cantilever was still loaded by applying

a vertical displacement to the end section, while twisting of the end section was also restrained (Fig. 10). As previously explained, the cantilever setup was devised to be representative of the portion of a beam between the connection and the point of inflection in a typical moment resisting frame. The mesh size was maintained at 20x20 mm^2. Eight-noded shell elements with reduced integration and five nodal degrees of freedom (S8R5) were again used.

Five different prototype sections, listed in Table 2, were considered and independently optimized. The same amount of material as used in the 'standard' commercial channel was used for all cross-sections (i.e. the same total developed plate width $L = 415\,mm$ and the same thickness $t = 1.5\,mm$). The independent design variables are listed in Table 2 and consisted of cross-sectional dimensions, stiffener locations and the angles included between various plate segments. The intermediate stiffeners were always comprised of two 10 mm legs with an intersecting angle of 60°. It is noted that, for each prototype in Table 2, one of the independent variables has already been eliminated by using the constraint of a constant developed length. All cross-sections were required to meet the dimensional restrictions determining the range of validity of the EN1993-1-3 specifications. These restrictions, also listed in Table 2, pertain to plate slenderness limits as well as limit values on the relative dimensions of the cross-section and were included as constraints on the optimisation problem. These restrictions were imposed in order to obtain cross-section which can be validly designed using EC3. They are not considered very stringent and in most cases were not critical to the optimization process. However, an important practical constraint was also imposed on all cross-sections: in order to allow the section to support the roof or floor diaphragm above and be screw-connected to it, a minimum flat flange width (indicated by the symbol 'b' for prototypes 1-4 and 'c' for prototype 5) of 50 mm was specified. This value was obtained after consultation with the industrial partner on the project. For the purpose of manufacturing the section, the lip stiffener also needed to have a minimum length, since a very short lip cannot be rolled or brake-pressed. For

prototypes 1-4 the EC3 requirement that c/b ≥ 0.2 (EN1993-1-3 Clause 5.2), combined with a minimum flange width of 50 mm, automatically resulted in a minimum lip length of 10 mm, which is acceptable as an absolute minimum. For prototype 5, however, the requirement of a minimum lip length (d ≥ 15 mm) needed to be explicitly enforced. Finally, a maximum length b ≤ 50 mm was imposed on prototype 5 in order to leave enough flat web width to accommodate a bolted or screwed connection at the member ends.

After optimizing the cross-sections for a thickness of 1.5 mm, two additional optimization studies were carried out, where the wall thickness of the channel was increased to 3 mm and 5 mm, respectively, in order to be able to draw conclusions over a wider range of wall slenderness values.

The measured material stress-strain curve shown in Fig. 6 was used in the optimization process. The corresponding yield stress f_y, elastic modulus E and Poisson's ratio ν were 427 MPa, 200 *GPa* and 0.3, respectively.

The optimisation procedure aimed to optimise each CFS cross-section prototype with respect to its energy dissipation $E(\boldsymbol{X})$ over the load history up to a drift ratio of 4%. This is the rotation capacity required for Special Moment Frames (SMF) according to AISC Seismic Provisions (2016) and allows a consistent comparison.

The optimisation problem was formulated mathematically as follows:

$$\max \qquad E(\boldsymbol{X}) \tag{3}$$

$$x_i^L \le x_i \le x_i^U, \qquad (i = 1, \cdots, n) \tag{4}$$

where $\boldsymbol{X}$ denotes the vector containing the independent cross-sectional variables x_i listed in Table 2. $\boldsymbol{X}^U$ and $\boldsymbol{X}^L$ indicate the upper and lower bounds, respectively, of the design variables which are subject to constraints.

Table 2. Selected prototypes, design variables and constraints

Prototype	Prototype section	Design variables	Initial values of design variables	Constraints	Comments
①	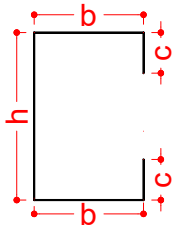	$x_1=c/b$ $x_2=b/L$	$x_1=0.227$ $x_2=0.181$	$0.2\le c/b\le 0.6$ $b/t\le 60$ $c/t\le 50$ $h/t\le 500$ $b\ge 50$	EN1993-1-3 Clause 5.2 practical
②	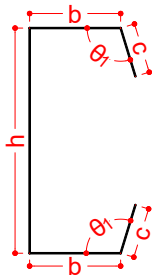	$x_1=c/b$ $x_2=b/L$ $x_3=\vartheta_1$	$x_1=0.227$ $x_2=0.181$ $x_3=\pi/2$	$0.2\le c/b\le 0.6$ $b/t\le 60$ $c/t\le 50$ $h/t\le 500$ $\pi/4\le\vartheta_1\le 3/4\pi$ $b\ge 50$	EN1993-1-3 Clause 5.2 practical
③	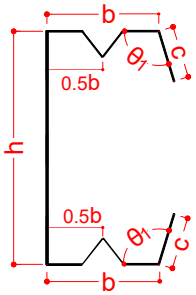	$x_1=c/b$ $x_2=b/L$ $x_3=\vartheta_1$	$x_1=0.227$ $x_2=0.181$ $x_3=\pi/2$	$0.2\le c/b\le 0.6$ $b/t\le 60$ $c/t\le 50$ $h/t\le 500$ $\pi/4\le\vartheta_1\le 3/4\pi$ $b\ge 50$	EN1993-1-3 Clause 5.2 practical
④	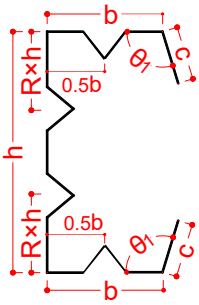	$x_1=c/b$ $x_2=b/L$ $x_3=R$ $x_4=\vartheta_1$	$x_1=0.227$ $x_2=0.181$ $x_3=0.2$ $x_4=\pi/2$	$0.2\le c/b\le 0.6$ $b/t\le 60$ $c/t\le 50$ $h/t\le 500$ $\pi/4\le\vartheta_1\le 3/4\pi$ $0.1\le R\le 0.4$ $b\ge 50$	EN1993-1-3 Clause 5.2 practical practical
⑤	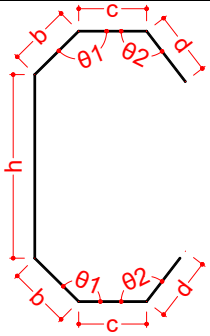	$x_1=\vartheta_1$ $x_2=\vartheta_2$ $x_3=b$ $x_4=c$ $x_5=d$	$x_1=7/12\pi$ $x_2=3/4\pi$ $x_3=40$ $x_4=40$ $x_5=50$	$h/t\le 500$ $7/12\pi\le\vartheta_1\le 5/6\pi$ $\pi/4\le\vartheta_2\le 3/4\pi$ $b\le 50$; $d\ge 15$ $c\ge 50$	EN1993-1-3 practical practical practical

4.2 Optimisation techniques

The optimisation framework made use of the Particle Swarm Optimisation (PSO) method. This global optimisation algorithm is population-based and does not need any gradient information, which makes it suitable for solving complex problems with high non-linearity. PSO generally possesses better computational efficiency in terms of both speed and memory requirements compared to conventional Genetic Algorithm (GA) techniques (Hassan et al. 2005, Jeong et al. 2009).

PSO is inspired by the swarming behaviour of biological populations such as flocks of birds or schools of fish. An initial population of solutions is randomly selected and the solutions are then optimised by updating subsequent generations, but unlike GA this is done without using any evolution operators such as crossover or mutation. The potential solutions in PSO, called particles, move in the problem space by following the current optimum particles to search for the global optimal solution. A swarm is thus comprised of N particles moving around a D-dimensional search space. The position and velocity vectors of the i^{th} particle are $\boldsymbol{\rho}_i = \left\{\rho_{i1}, \rho_{i2}, ..., \rho_{ij}, ..., \rho_{iD}\right\}$ and $\boldsymbol{V}_i = \left\{v_{i1}, v_{i2}, ..., v_{ij}, ..., v_{iD}\right\}$, respectively, where $i = 1,2,3,...N$. In each iteration, the i^{th} particle updates its position and velocity based on a combination of its personal best position over its history and the position of the particle within the swarm with the best position in the previous iteration. This can mathematically be described as:

$$\boldsymbol{V}_i^{k+1} = w \cdot \boldsymbol{V}_i^k + c_1 \cdot r_1 \cdot \left(\boldsymbol{P}_{best,i}^k - \boldsymbol{\rho}_i^k\right) / \Delta t + c_2 \cdot r_2 \cdot \left(\boldsymbol{G}_{best}^k - \boldsymbol{\rho}_i^k\right) / \Delta t \tag{5}$$

$$\boldsymbol{\rho}_i^{k+1} = \boldsymbol{\rho}_i^k + \boldsymbol{V}_i^{k+1} \cdot \Delta t \tag{6}$$

where the subscripts i and k denote the particle and the iteration number, respectively, and Δt is the time increment. $\boldsymbol{P}_{best,i}^k = \left\{p_{i1}^k, p_{i2}^k, ..., p_{iD}^k\right\}$ represents the best position of the i^{th} particle over its history up to iteration k, while $\boldsymbol{G}_{best}^k = \left\{g_1^k, g_2^k, ..., g_D^k\right\}$ indicates the position of the best particle in the swarm in iteration k. The cognitive parameter c_1 indicates the degree of confidence in the

solution $P_{best,i}$ obtained from each individual particle. The parameter c_2 is a social parameter to reflect the confidence level that the swarm as a whole has reached a favourable position. In addition, the factors r_1 and r_2 are independent random numbers uniformly distributed between 0 and 1, adding a random search aspect to the algorithm. Finally, w is an inertial weight factor used to preserve part of the previous velocity of the particles, in order to improve the convergence of the optimisation process. PSO has the added advantage that the optimization constraints (Eq. 4) can easily be accommodated by restricting the search space and defining appropriate boundaries.

The initial position and velocity vectors were randomly distributed throughout the design space for each particle of the swarm. Eqs.(7) and (8) are therefore used to obtain these vectors. For each design variable $\boldsymbol{X}_i$, with a lower bound $\boldsymbol{X}_i^L$ and an upper bound $\boldsymbol{X}_i^U$ (as shown in Eq.(4)), the following equations were used to obtain the initial position and velocity vectors:

$$\boldsymbol{X}_i^0 = \boldsymbol{X}_i^L + r\left(\boldsymbol{X}_i^U - \boldsymbol{X}_i^L\right) \tag{7}$$

$$\boldsymbol{V}_i^0 = \frac{r\left(\boldsymbol{X}_i^U - \boldsymbol{X}_i^L\right)}{\Delta t} \tag{8}$$

where r represents a random number between 0 and 1.

It is worth mention that when the position value $\boldsymbol{\rho}_i^{k+1}$ of a particle is outside the design domain [$\boldsymbol{X}_i^L$, $\boldsymbol{X}_i^U$], the position value will be set as the upper or lower bound ($\boldsymbol{X}_i^L$ or $\boldsymbol{X}_i^U$) to pull it back to the feasible region..

Fig. 16 illustrates the flowchart of the proposed optimisation method, which had to overcome the difficulty of linking the detailed FE simulations in ABAQUS (2014) to the PSO algorithm in Matlab (2011). In each iteration the PSO algorithm generated new input data, i.e. new position vectors ρ_i containing values of the basic variables which determine the cross-sectional geometry (as listed in Table 2). This data was then transmitted to the ABAQUS pre-processing module to create

the cantilever beam model. The entire FE analysis was controlled using a Python script which consisted of the following steps:

(1) The FE model of a 1400 mm long cantilever beam was generated using the cross-sectional dimensions generated by the PSO algorithm. The material stress-strain curve shown in Fig. 6 was used. Boundary conditions as previously described in Section 3.2 and illustrated in Fig. 10 were applied to the FE model and a vertical displacement was imposed at the cantilever tip.

(2) A linear elastic buckling analysis was conducted in ABAQUS. The normalized nodal displacements of the most critical buckling mode were extracted and used as the shape of the initial geometric imperfection. This shape was then scaled to obtain an imperfection amplitude of 0.94 times the thickness of the cross-section, which is the 50% cumulative distribution value for the distortional imperfection as measured by Schafer and Pekoz (1998). In order to automate the optimization process this amplitude was chosen irrespective of whether the local mode or the distortional mode was critical, in the knowledge that this value might be slightly conservative for the local mode.

(3) The Standard solver of ABAQUS was used to carry out a GMNIA FE analysis for each PSO particle. The dissipated energy $E(\boldsymbol{X})$ of each particle was then extracted from the ABAQUS output files using its post-processing module.

(4) The data extracted in the previous step were returned to the PSO algorithm and a new particle swarm was generated based on Eqs. (5) and (6). Subsequently, a new iteration was started from step 1 above.

The number of iterations was taken as 100 for all prototype sections. To obtain good convergence the population of the swarm was set to 10 particles for prototypes ① to ③ and 15 particles for prototypes ④ and ⑤, to accommodate the fact that these latter prototypes contained more design variables. The maximum and minimum inertial weight factors were chosen as 0.95 and 0.4,

respectively. Larger values of the weight factor were used in the initial stages of the optimisation, as this promotes global searching over a large area of the parameter domain. Conversely, a small value of the weight factor tends to localize the search pattern, a technique which can be used to accelerate the convergence in the later stages. The weight factor was varied linearly over the iterations between the above values. These choices for the PSO parameters were based on previous experience by the authors (Ye et al. 2016a) and on recommendations by Perez and Behdinan (2007). Figure 17 shows a typical convergence diagram and illustrates that there was no obvious increase of the objective value (i.e. the energy dissipation capacity) after about 60 iterations. This confirms that the number of iterations used in this study was adequate.

Due to the substantial computational effort required, the non-linear FE analyses were conducted on the High Performance Computing system Iceberg at the University of Sheffield.

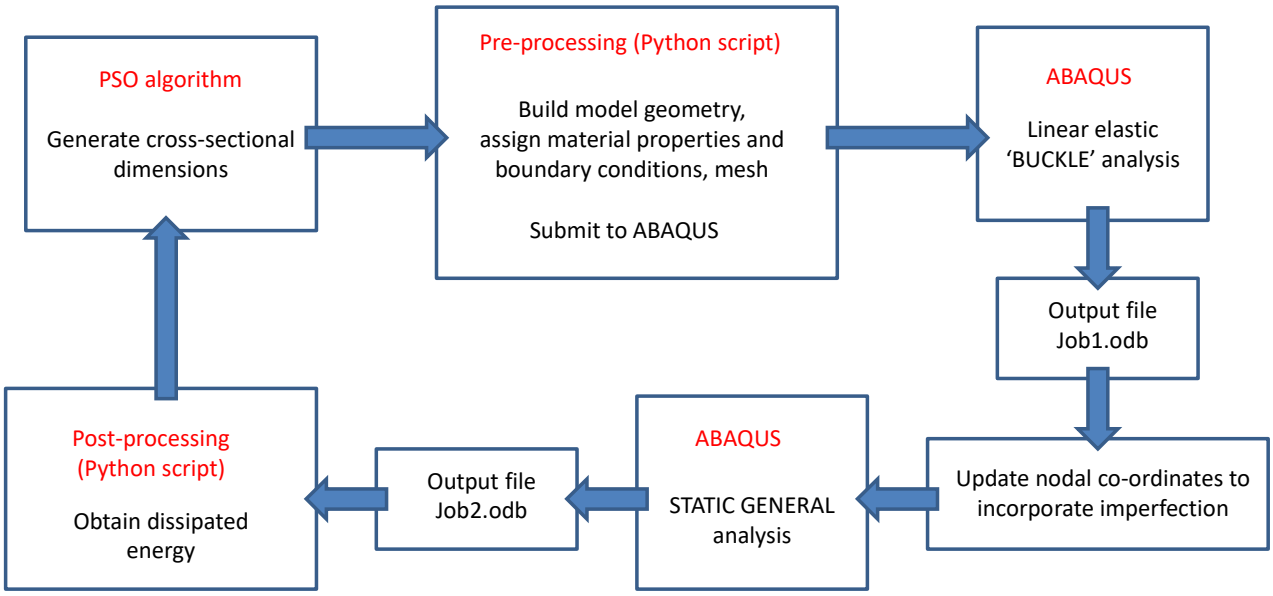

Fig. 16. Flowchart of the proposed optimisation framework for maximum dissipated energy

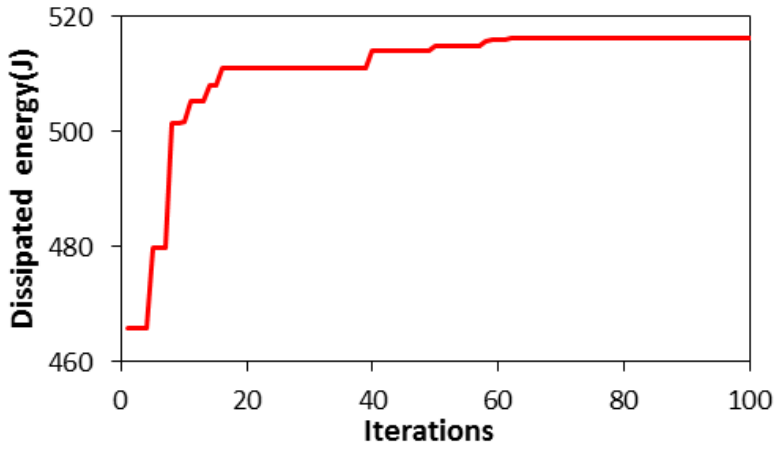

Fig. 17. Typical iteration history

5 Optimisation results and discussions

Table 3 summarizes the dimensions of the cross-sectional shapes obtained from the optimization process (with reference to Table 2 for the symbols used) and compares them with the standard lipped channel section with the same amount of material taken as a starting point.

Table 3. Dimensions, energy dissipation and moment capacity of optimum CFS cross-sections of different prototypes and thicknesses

Plate Thickness	Prototypes	h (mm)	b (mm)	c (mm)	d (mm)	R	θ_1	θ_2	E (J)	M_{max} (kN.m)	$\frac{E}{E(\text{standard})}$	$\frac{M_{max}}{M_{max}(\text{standard})}$
1.5	standard	231	75	17					329	16.6	1.00	1.00
	Type ①	255	50	30					407	18.3	1.24	1.10
	Type ②	255	50	30			82		413	18.3	1.26	1.10
	Type ③	249	50	18			89		441	18.6	1.34	1.12
	Type ④	205	50	25		0.2	45		512	19.4	1.56	1.17
	Type ⑤	183	41	50	25		126	135	508	20.1	1.55	1.21
3	standard	231	75	17					963	45.0	1.00	1.00
	Type ①	255	50	30					1199	47.5	1.25	1.05
	Type ②	366	50	30			90		1199	47.5	1.25	1.05
	Type ③	265	50	10			92		1181	47.8	1.23	1.06
	Type ④	235	50	10		0.1	77		1199	45.2	1.24	1.00
	Type ⑤	189	48	50	15		105	135	1343	48.6	1.39	1.08
5	standard	231	75	17					2189	78.6	1.00	1.00
	Type ①	276	50	20					2467	87.3	1.13	1.11
	Type ②	278	50	19			87		2474	87.0	1.13	1.11
	Type ③	265	50	10			78		2430	86.1	1.11	1.10
	Type ④	235	50	10		0.1	45		2237	79.8	1.02	1.02
	Type ⑤	169	48	60	15		105	135	2252	79.4	1.03	1.01

The resulting cross-sectional geometries are also graphically presented in Fig. 18, while Fig. 19 presents a comparison between the dissipated energies of the various optimized prototypes.

Thickness (mm)	Prototypes				
	①	②	③	④	⑤
1.5					
3					
5					

Fig. 18. Optimized cross-sections (to scale)

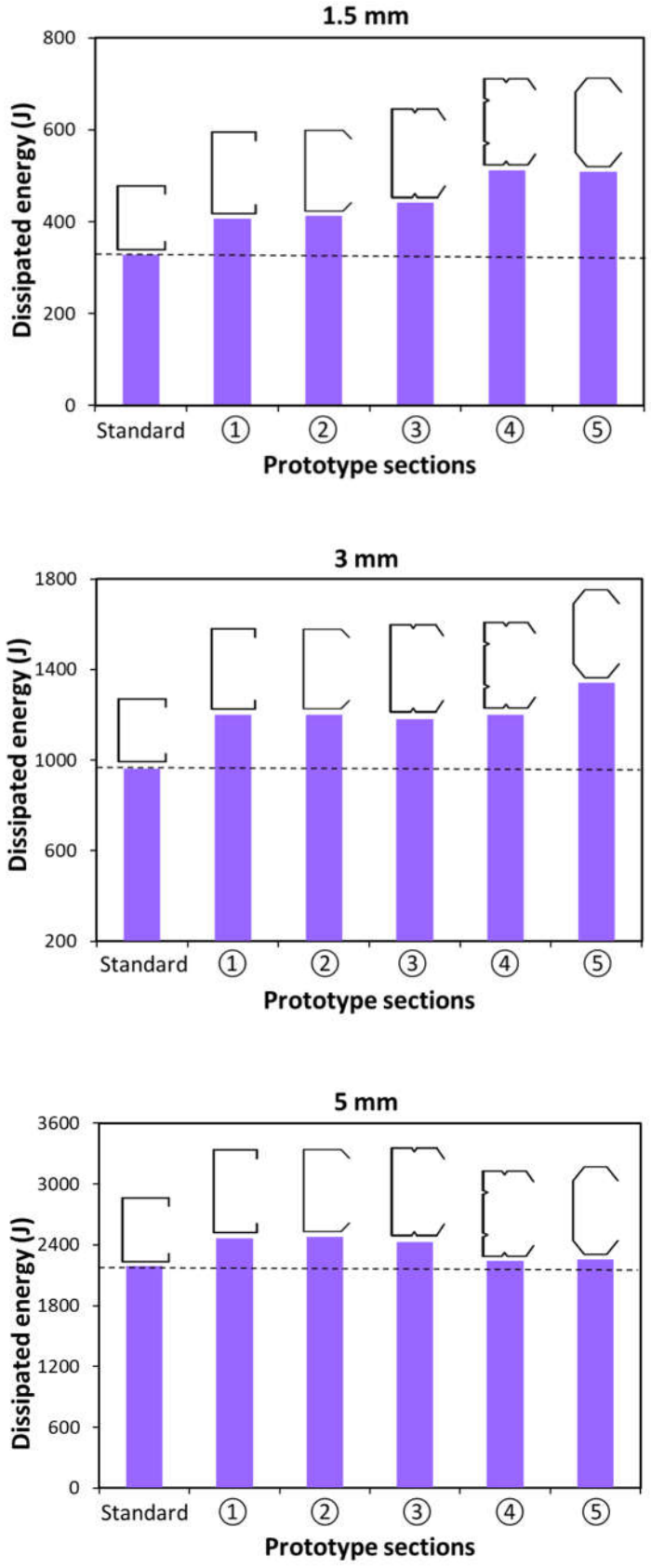

Fig. 19. Maximum dissipated energy of prototypes at 4% drift ratio

A number of interesting observations can be made from Figs. 18-19:

- By simply changing the relative dimensions of the standard commercial channel an optimized section could be obtained (prototype 1) with noticeably better energy dissipation characteristics. The gains for thicknesses of 1.5 mm, 3 mm and 5 mm were 24%, 25% and 13%, respectively. At the same time, the peak moment capacity was also improved by 5-11%.
- For all thicknesses, the lipped channel without any intermediate flange or web stiffeners strived to increase its energy dissipation capacity by increasing the depth of the web, while at the same time shortening the flange (note that the total developed length of the cross-section needed to remain constant). This has the combined effect of (1) increasing the peak moment, and (2) delaying the distortional buckling mode until larger deformations have taken place. For all thicknesses considered and over the range of prototypes 1-4, the flanges took on the minimum value of 50 mm, which was set as the minimum required width to allow for connections to the floor or roof diaphragm.
- Allowing the angle between the lip stiffener and the web to vary in prototype 2 did not result in a noticeable effect on either the ultimate moment capacity or the energy dissipation capacity of the optimized section. The optimum angles resulting from the process were all close to 90^{o}.
- For a thickness of 1.5 mm, the addition of flange stiffeners or combined flange and web stiffeners significantly improved the energy dissipation capacity. Prototype 3 had an 8% higher energy dissipation capacity than prototype 1, while this number was 26% for prototype 4. The stiffeners are effective in suppressing cross-sectional instability, resulting in a slightly increased peak moment (as indicated in Table 3). At the same time these cross-sections also exhibited an increased ductility (as indicated in Fig. 13 and defined on the basis of a 20% drop in capacity), which is a direct result of the stiffeners delaying and mitigating

the stiffness degradation due to buckling. It is noted that the stiffeners were accounted for in the total developed length of the cross-section and that, therefore, the depth of the optimized prototypes 3 and 4 is less than that of prototype 1. Nevertheless, prototype 3 has a 2% higher ultimate moment capacity than prototype 1, while this number is 6% for prototype 4.

- For a thickness of 3 mm, adding intermediate stiffeners to the section did not have a significant effect on the ultimate moment capacity of prototype 3 compared to prototype 1, while it actually slightly reduced the ultimate moment capacity in prototype 4 (by 5%). This is a result of the reduction in section depth needed to accommodate the stiffeners, while the stiffeners become less effective as the width-to-thickness ratios of the web and flange are reduced. However, the stiffeners still played a beneficial role in the post-peak behaviour of the cross-section by mitigating the loss in stiffness due to buckling. Interestingly, the net result of these two opposing effects is zero and no significant loss or gain in energy dissipation was obtained by adding intermediate stiffeners.
- For a thickness of 5 mm, adding intermediate stiffeners to the section resulted in a slight reduction in energy dissipation capacity. Prototype 3 dissipated 1.5% less energy than prototype 1, while prototype 4 dissipated 9% less energy than prototype 1. This is mainly due to the fact that sacrificing some of the depth of the section in order to accommodate the stiffeners led to a slight reduction in peak moment capacity of 1.4% for prototype 3 and 9% for prototype 4. In this context it is noted that EN1993-1-1 (2005) classifies the optimized prototype 1 section with a thickness of 5 mm as a Class 2 cross-section. While this classification does not account for distortional instability, it provides an indication of the limited effectiveness of intermediate stiffeners in increasing the ultimate moment capacity.

- The folded flange section (prototype 5) in general performed well in terms of energy dissipation. For a thickness of 1.5 mm prototype 5 provided a slightly less efficient solution than the prototype with flange and web stiffeners (prototype 4). For a thickness of 3 mm it provided the overall optimum solution, as it combines a beneficial section depth with a defence against local and distortional buckling due to the segmental shape. For a thickness of 5 mm, however, prototype 5 did not dissipate as much energy as most of the other optimum prototypes, although the differences were marginal.

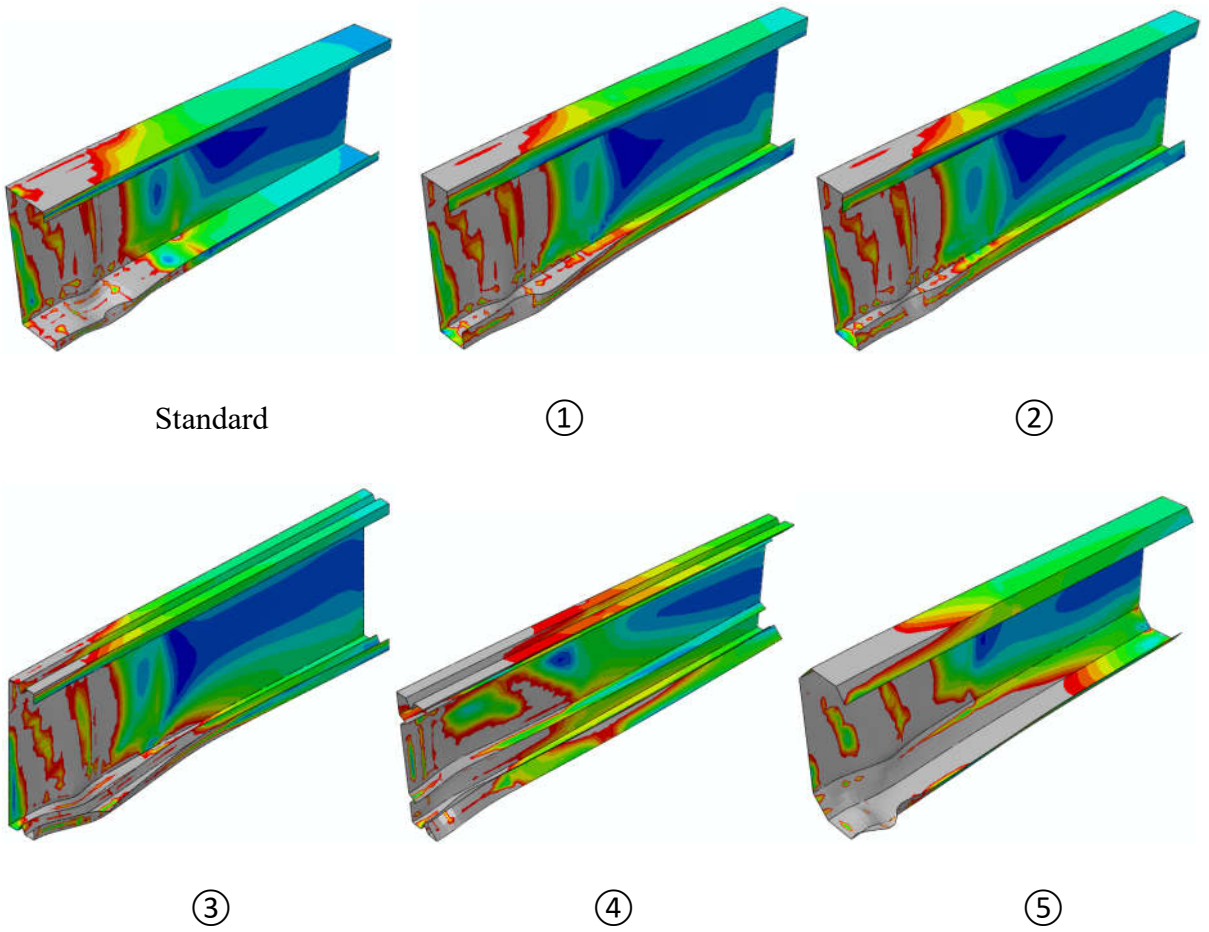

Fig. 20. Deformed shape and distribution of von Mises stress at a drift ratio of 4% for t = 1.5 mm

Fig. 20 illustrates the deformed shapes of all optimum prototypes with thickness t = 1.5 mm at a drift ratio of 4% (i.e. the SMF limit). The von Mises stress distribution is also shown with grey areas indicating yielding. It is seen that the cross-sections all fail in either a predominantly local (prototypes 1 and 2) or predominantly distortional mode (prototypes 3, 4 and 5) and exhibit significant localized yielding near the fixed end support. The beam rotations therefore become localized in a hinge-like zone near the support.

6. Conclusions

This paper presents a study of the energy dissipation capacity and ductility of CFS channel sections. These parameters are of the utmost importance in seismic applications, while comparatively little attention has been devoted to them in previous work.

An optimization framework is presented which integrates a PSO algorithm with detailed GMNIA finite element analyses in order to develop CFS cross-sections with optimum energy dissipation characteristics. A number of practical construction and manufacturing constraints were also considered. Five different prototypes were considered in order to study the effect of adding intermediate flange and web stiffeners and allowing inclined lip stiffeners.

It was found that for the slender cross-sections with a thickness of 1.5 mm, corresponding to a web slenderness (i.e. width-to-thickness ratio) of 185 and a flange slenderness of 33, a substantial increase in energy dissipation (of up to 26%) could be obtained by adding intermediate web and flange stiffeners. This was a result of the stiffeners both increasing the ultimate capacity and mitigating the post-peak stiffness degradation. For web and flange slenderness values of 93 and 17, respectively, a turning point was reached where adding intermediate stiffeners slightly reduced the peak moment, while marginally improving the post-peak behaviour, resulting in no net gain in dissipated energy. For stockier sections, the addition of intermediate stiffeners is not expected to

result in a more optimum solution. Instead, maximizing the depth of the cross-section and minimizing the flange width leads to better energy dissipation behaviour.

The 'folded flange' section performed well in the high-to-medium slenderness range, where it provided the overall optimum or slightly below-optimum solution.

Acknowledgments

This work was supported by EPSRC grant EP/L019116/1. The authors would like to thank the EPSRC for their financial support.

References

ABAQUS Inc. (2014). *ABAQUS/CAE User's Guide, v6.14*, Pawtucket, USA.

ANSI/AISC 341-16 (2016), *Seismic provisions for structural steel buildings*, American institute of steel construction (AISC), Illinois, USA.

ASTM E2126 (2009). *Standard test methods for cyclic (reversed) load test for shear resistance of vertical elements of the lateral force resisting systems for buildings*. American Society for Testing and Materials, West Conshohocken, USA.

Becque, J. (2014). "Local-overall interaction buckling of inelastic columns: A numerical study of the inelastic Van der Neut column." *Thin-Walled Structures*, 81 (special issue), 101-107.

Becque, J., and Rasmussen, K.J.R. (2009a). "A numerical investigation of local-overall interaction buckling of stainless steel lipped channel columns." *Journal of Constructional Steel Research*, 65 (8-9), 1685-1693.

Becque, J., and Rasmussen, K.J.R. (2009b). "Numerical investigation of the interaction of local and overall buckling of stainless steel I-columns." *ASCE Journal of Structural Engineering*, 135 (11), 1349-1356.

Calderoni, B., De Martino, A., Formisano, A., and Fiorino, L. (2009). "Cold formed steel beams under monotonic and cyclic loading: Experimental investigation.", *Journal of Constructional Steel Research*, 65, 219-227.

CEN (2005). EN1993-1-1 *Eurocode3: Design of steel structures, Part 1.1: General rules and rules for buildings*, European Committee for Standardization, Brussels.

CEN (2005). EN1993-1-3 *Eurocode 3: Design of steel structures, Part 1.3: Supplementary rules for cold formed members and sheeting*, European Committee for Standardization, Brussels.

CEN (2005). EN1998-1 *Eurocode 8: Design of structures for earthquake resistance, Part 1: General rules, seismic actions and rules for buildings*, European Committee for Standardization, Brussels.

Gardner, L., and Ashraf, M. (2006). "Structural design for non-linear metallic materials.", *Engineering Structures*, 28, 926-934.

Haidarali, M.R., and Nethercot, D.A. (2011). “Finite element modelling of cold-formed steel beams under local buckling or combined local/distortional buckling.”, *Thin-Walled Structures*, 49, 1554-1562.

Hassan, R., Cohanim, B., De Weck, O.,Venter, G. (2005). “A comparison of particle swarm optimization and the genetic algorithm.”, *Proceedings of the 1st AIAA Multidisciplinary Design Optimization Specialist Conference*, 2005, 18-21.

Jeong, S., Hasegawa, S., Shimoyama, K., and Obayashi, S. (2009) “Development and investigation of efficient GA/PSO-hybrid algorithm applicable to real-world design optimization.”, *Computational Intelligence Magazine*, IEEE, 4, 36-44.

Leng, J., Li, Z., Guest, J.K., and Schafer B.W. (2014). “Shape optimization of cold-formed steel columns with fabrication and geometric end-use constraints.”, *Thin-Walled Structures*, 85, 271-290.

Liu, H., Igusa, T., and Schafer, B.W. (2004). “Knowledge-based global optimization of cold-formed steel columns.”, *Thin-Walled Structures*, 42, 785-801.

Ma, W., Becque, J., Hajirasouliha, I., and Ye, J. (2015). “Cross-sectional optimization of cold-formed steel channels to Eurocode 3.” *Engineering Structures*, 101, 641-651.

Mathworks Inc. (2011), Matlab R2011a.

Nithyadharan, M., and Kalyanaraman, V. (2012). “Behaviour of cold-formed steel shear wall panels under monotonic and reversed cyclic loading.” *Thin-Walled Structures*, 60, 12-23.

Padilla-Llano, D.A., Moen, C.D., and Eatherton, M.R. (2014). “Cyclic axial response and energy dissipation of cold-formed steel framing members.”, *Thin-Walled Structures*, 78, 95-107.

Pan, P., Ohsaki, M., and Tagawa, H. (2007). “Shape optimization of H-beam flange for maximum plastic energy dissipation.”, *Journal of Structural Engineering*, ASCE, 133, 1176-1179.

Perez, R. E., and Behdinan, K. (2007). “Particle swarm approach for structural design optimization.” Computers & Structures, 85(19), 1579-1588.

Sabbagh, A.B., Petkovski, M., Pilakoutas, K., and Mirghaderi, R. (2012). “Development of cold-formed steel elements for earthquake resistant moment frame buildings.”, *Thin-Walled Structures*, 53, 99-108.

Schafer, B.W., Li, Z., and Moen, C.D. (2010). “Computational modelling of cold-formed steel.” *Thin-Walled Structures,* 48 (10), 752-762.

Schafer, B.W., and Pekoz, T. (1998). “Computational modeling of cold-formed steel: characterizing geometric imperfections and residual stresses”, *Journal of Constructional Steel Research*, 47, 193-210.

Tian, Y.S., Lu, J. (2004). “Minimum weight of cold-formed steel sections under compression.”, *Thin-Walled Structures*, 42, 515-532.

van der Neut, A. (1969). “The interaction of Local Buckling and Column Failure of Thin-walled Compression Members.” *Proceedings of the 12th International Congress on Applied Mechanics*, 389-399.

Ye, J. (2016). *More efficient cold-formed steel elements and bolted connections.* PhD thesis, The University of Sheffield.

Ye, J., Hajirasouliha, I., Becque, J., and Eslami, A. (2016a). "Optimum design of cold-formed steel beams using particle swarm optimization method." *Journal of Constructional Steel Research*, 122, 80-93.

Ye, J., Hajirasouliha, I., Becque, J., and Pilakoutas, K. (2016b). "Development of more efficient cold-formed steel channel sections in bending." *Thin-walled Structures*, 101, 1-13.

Yu, C., and Schafer, B.W. (2007) "Simulation of cold-formed steel beams in local and distortional buckling with applications to the direct strength method.", *Journal of Constructional Steel Research*, 63, 581-590.